

Phase-Amplitude Reduction-Based Imitation Learning

Satoshi Yamamori^a and Jun Morimoto^{a, b}

^aDepartment of Brain Robot Interface, ATR Computational Neuroscience Laboratories, Kyoto, Japan;

^bGraduate School of Informatics, Kyoto University, Kyoto, Japan

ARTICLE HISTORY

Compiled June 7, 2024

ABSTRACT

In this study, we propose the use of the phase-amplitude reduction method to construct an imitation learning framework. Imitating human movement trajectories is recognized as a promising strategy for generating a range of human-like robot movements. Unlike previous dynamical system-based imitation learning approaches, our proposed method allows the robot not only to imitate a limit cycle trajectory but also to replicate the transient movement from the initial or disturbed state to the limit cycle. Consequently, our method offers a safer imitation learning approach that avoids generating unpredictable motions immediately after disturbances or from a specified initial state. We first validated our proposed method by reconstructing a simple limit-cycle attractor. We then compared the proposed approach with a conventional method on a lemniscate trajectory tracking task with a simulated robot arm. Our findings confirm that our proposed method can more accurately generate transient movements to converge on a target periodic attractor compared to the previous standard approach. Subsequently, we applied our method to a real robot arm to imitate periodic human movements.

KEYWORDS

Imitation learning, Variational Inference, Learning Dynamical Systems

1

1. Introduction

In imitation learning approaches, a robot learns from human demonstration data to generate human-like motions [1–3]. Studies in imitation learning have shown that robots can imitate human expert movements, such as kendama (cup-and-ball) [4] and table tennis [5], skills that even humans need to acquire proficiency in. Recent advancements in deep learning have led to improvements in imitation learning performance [6–8], enabling flexible object manipulation [9]. However, collecting large-scale human movement data to generate a wide variety of motions demands significant effort. Thus, approximating the time series of human movements with a dynamical system to generate stable trajectories, even in cases where sufficient data is unavailable, can prove to be a valuable and extensively studied approach [10,11]. The limitation of conventional dynamical movement primitive (DMP) approaches is that they can accurately approximate human movement only around the limit cycle and cannot adequately

CONTACT Satoshi Yamamori. Email: yamamori@atr.jp

¹This is a preprint of an article submitted for consideration in ADVANCED ROBOTICS, copyright Taylor & Francis and Robotics Society of Japan; ADVANCED ROBOTICS is available online at <http://www.tandfonline.com/>.

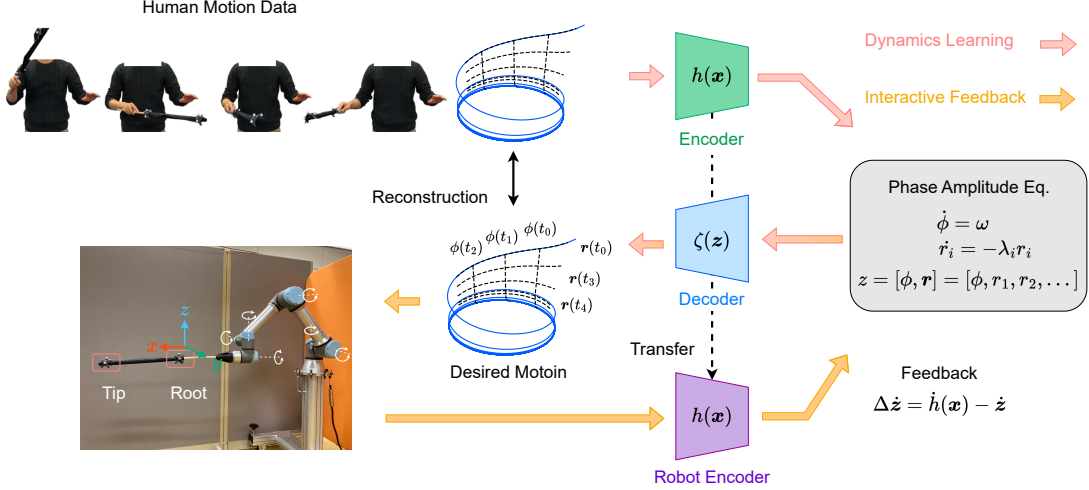


Figure 1. Phase-amplitude reduction-based imitation learning method. Our proposed method reconstructs a human trajectory, recorded by an optical motion capture system, using an encoder h and a decoder ζ . Human trajectory is encoded in a latent space that follows the phase-amplitude equation representing a linear system with a frequency term ω and an exponent term λ_i , which determines the trajectory’s amplitude r_i and phase ϕ . Phase ϕ represents a steady response continuing for a long time and r_i represents the transient response scaled by λ_i and converging to the origin. Encoder h projects the robot state to latent space. Feedback connection is provided to regulate the latent variables according to the robot state.

represent transient movements. As a result, the reproduced robot behavior deviates from the demonstration data in a transient phase.

This study proposes a novel imitation learning framework that uses the phase-amplitude reduction method. The phase-amplitude reduction theory, developed based on the phase-reduction theory [12], analyzes nonlinear oscillators and embeds the system state into a low-dimensional space [13]. Each subspace of the embedded latent space corresponds to a phase of a limit cycle and an amplitude component converging to the limit cycle, making it ideal for analyzing dynamic motion. Unlike the previous dynamical system-based imitation learning approach, the proposed method enables the robot to imitate not only a stable orbit but also the transient movement from the initial or disturbed state to the stable orbit. Consequently, the proposed method provides a safer imitation learning method that does not generate unpredictable motions after disturbances or given an initial state. First, we verified our proposed method by reconstructing a simple limit-cycle attractor. Then, we applied the proposed method to a real robot arm to imitate periodic human movements. We confirmed that our proposed method could more accurately generate transient movements to converge on a target periodic attractor than the previous standard approach [10,11]. As shown in Fig. 1, the proposed method uses a supervised learning framework based on variational inference to obtain an encoder-decoder that performs embedding and reconstruction from the demonstration data to the phase-amplitude space.

The proposed method comprises two components: 1) dynamics learning and 2) interactive feedback, aimed at assisting the robot in adhering to the desired trajectory obtained from human data. Besides the feedback from the desired dynamical system to the robot, the robot also provides feedback of its state to the latent space through the encoder network. The reduction in the phase-amplitude space reconstructs the transient response of human motion while retaining the function to represent the limit cycle.

This study validated that the proposed method can learn a simple limit cycle model, perform a lemniscate curve-following task for a 6DoF arm robot, and replicate baton waving behavior exhibited by a human on a real robot. The results demonstrate that the proposed method can

accurately reproduce the original dynamics, guide the robot toward the desired behavior, and successfully transition to a real robot. The contributions of this study are as follows:

- We proposed using the variational inference approach for stable learning of the encoder and decoder to imitate demonstrated movements.
- The proposed learning method was further equipped with the feedback mechanism from the robot to the latent dynamics to cope with external disturbances.
- The transient responses from an initial or disturbed state were successfully reconstructed in a simple limit cycle example and also in a tracking task of a simulated arm robot.
- We confirmed that the real arm robot could imitate demonstrated human movement by using the proposed learning method.

The remainder of this paper is organized as follows. Section II introduces related studies. Section III explains the proposed method. Section IV introduces the experimental setups. Section V presents the results on both the simulation and the real system. Finally, Section VI concludes this paper.

2. Related Works

2.1. *Trajectory-based imitation learning*

Approaches that generate trajectories using dynamical systems, such as DMP, have demonstrated the ability to produce reliable motion despite their simple mechanisms. Model-based imitation learning facilitates reinforcement, inverse reinforcement, and imitation learning because smooth curves can connect the initial and target points [14]. Additionally, the dynamics coupling approach between the real and target systems can modify systems that deviate from the desired dynamical system [15,16]. In this study, we construct a state feedback system in phase-amplitude space to enable trajectory tracking that considers the dynamic characteristics of the imitator.

2.2. *Latent representation in dynamics model*

This paper proposes a dynamic model-learning algorithm based on phase-amplitude reduction. This dynamics model is suitable for imitation learning since the robot can explicitly select the dynamic mode of the target to follow. Nonlinear dynamics learning through latent space has evolved from subspace identification methods [17] to include kernel methods [17], Koopman operators [18], Gaussian process regression [19,20], neural networks [21], methods restricted to stable dynamical systems [22,23], and mixed Gaussian distributions [24], among others. Notably, the phase-amplitude equation is classified as the Hammerstein-Wiener model, which sandwiches a linear dynamical system between static nonlinear functions. A similar approach for imitation learning involves neural networks and Koopman operators [25].

3. Methods

3.1. *Phase-amplitude Reduction Latent Dynamics*

As illustrated in Fig. 1, our proposed method enables a robot to learn the representation of a latent dynamical system capable of imitating human movement trajectories. Specifically, encoder and decoder networks were trained to represent the latent dynamical systems using phase-amplitude reduction. To train these networks, we employed the variational inference

framework. The encoder network takes physical observation space inputs, such as position, orientation, and velocity of the end-effector position.

3.1.1. Phase-Amplitude Reduction

In the proposed approach, we approximate a demonstrated human movement trajectory by a continuous-time dynamical system:

$$\dot{\mathbf{x}} = F(\mathbf{x}), \quad (1)$$

where $\mathbf{x} \in \mathbb{R}^N$ is the state variable and $F(\mathbf{x})$ denotes a vector field in the state space. Assuming the autonomous dynamical system converges to a stable closed orbit, the nonlinear system can be reduced to the phase-amplitude equation [13] through the mapping $\mathbf{z} := [\phi, \mathbf{r}] = h(\mathbf{x})$, where the dynamics of the latent variable \mathbf{z} is defined as:

$$\dot{\mathbf{z}} = f(\mathbf{z}) = [\omega, -\lambda \odot \mathbf{r}],$$

where f is the latent dynamics vector field, the latent variable $\mathbf{z} \in \mathbb{R}^M$ comprises the phase $\phi \in \mathbb{R}$ and amplitude $\mathbf{r} \in \mathbb{R}^{M-1}$ with the characteristic frequency as well as exponents $\omega > 0$ and $\lambda > 0$, and the \odot is the element-wise multiplication. For the phased-amplitude dynamics, the following solution can be analytically derived $\phi(t) = \phi(0) + \omega t$, $\mathbf{r}(t) = \exp(-\lambda t) \odot \mathbf{r}(0)$; Therefore, the phase variable ϕ represents a steady response whereas the amplitude variable \mathbf{r} represents a transient response.

The initial value set $\mathbf{x}(\phi)$, the isochron, is mapped onto the same phase ϕ of the limit cycle. Similarly, the amplitude \mathbf{r} represents the level set in the basin of the limit cycle attraction, the isostable. This is, the phase ϕ indicates the clock time on the limit cycle and the amplitude \mathbf{r} indicates the distance from the limit cycle. The function h maps the coordinate of the state to the phase-amplitude space. Considering the latent space dimension is smaller than the system dimension, i.e., $M < N$, the latent dynamics representation can be referred to as a phase-amplitude "reduction".

If time t is sufficiently large, with $\lambda > 0$, the each elements of amplitude \mathbf{r} asymptotes to 0. Therefore, transient responses that are faster than the variable \mathbf{z} can be ignored as they presumably stay near the origin for the timescale of the phase-amplitude system response characterized by the inverse time constant λ . Therefore, observable \mathbf{x} is reconstructed by learning a decoder $\hat{\mathbf{x}} = \zeta(\mathbf{z})$ from the latent variable \mathbf{z} to observable \mathbf{x} .

This study aims to reconstruct the human demonstration data based on the phase-amplitude dynamics f by learning the encoder h and decoder ζ , as shown in Fig. 1. The characteristic frequency ω and characteristic exponent λ , which is the inverse time constant, can be estimated using time-series analysis, such as Fast Fourier Transform (FFT) or autocorrelation analysis.

3.1.2. Interactive Feedback

Here, as suggested in [15], we introduce a feedback control strategy by coupling the phase-amplitude dynamics with the observed sensor inputs (Fig. 1). We introduced a weakly coupled system of feedback on the robot system $G(y, u)$ with latent dynamical system f , described as:

$$\dot{\mathbf{y}} = G(\mathbf{y}, \mathbf{u}), \mathbf{u} = K(\zeta(\mathbf{z}) - \mathbf{y}) \quad (2)$$

$$\dot{\mathbf{z}} = f(\mathbf{z}) + g(\dot{h}(\mathbf{y}) - \dot{\mathbf{z}}), \quad (3)$$

where $\mathbf{y} \in \mathbb{R}^N$ is the robot state variable, $\mathbf{u} \in \mathbb{R}^L$ and $\mathbf{K} \in \mathbb{R}^{L \times N}$ are the control input and gain, respectively. g is the feedback gain. The encoder h converts the robot state \mathbf{y} into the latent variable \mathbf{z} , and the decoder ζ reconstructs the desired trajectory, as shown in Fig. 1.

3.2. Encoder-Decoder Learning

The proposed method adopts the Kalback–Libler (KL) divergence minimization based on variational inference. Similar to the β variational autoencoder (β -VAE) [26], encoder h and decoder ζ were learned for reconstructing the human trajectory \mathbf{x} through latent \mathbf{z} variables (Fig. 1). The variational inference approach estimates the posterior distribution $q(Z|X)$ and the probabilistic model distribution $p(Z)p(X|Z)$ given data distribution $p(X)$ by alternately updating these distributions to minimize the KL divergence $\text{KL}[p(X)q(Z|X)||p(Z)p(X|Z)]$. The graphical model of data \mathbf{x} and latent variables \mathbf{z} can be measured using $\text{KL}[q_1|p_1]$, as shown on the left side of Fig. 2 (a). Here, we consider the T length time series of observations $\mathbf{X} = \{\mathbf{x}_0, \mathbf{x}_1, \dots, \mathbf{x}_T\}$ and latents $\mathbf{Z} = \{\mathbf{z}_0, \mathbf{z}_1, \dots, \mathbf{z}_T\}$ and the following:

$$\min_{h, \zeta} \text{KL}[q|p], \quad (4)$$

$$q(\tau) = p(\mathbf{X}) \cdot e(\mathbf{z}_0|\mathbf{x}_0) \cdot \prod_{k=1}^T m_1(\mathbf{z}_k|\mathbf{z}_0), \quad (5)$$

$$p(\tau) = p(\mathbf{z}_0) \cdot d(\mathbf{x}_0|\mathbf{z}_0) \cdot \prod_{k=1}^T m_1(\mathbf{z}_k|\mathbf{z}_0)d(\mathbf{x}_k|\mathbf{z}_k), \quad (6)$$

where $\tau = \{\mathbf{x}_0, \mathbf{z}_0, \dots, \mathbf{x}_T, \mathbf{z}_T\}$ is a trajectory of observation \mathbf{x} . e, d and m_1 denote the probabilistic models of the encoder, decoder, and latent dynamical system, respectively. $p(\mathbf{X})$ denotes data distribution and $p(\mathbf{z}_0)$ is the prior. To make the learning procedure robust against the outlier, we adopted the Laplace distribution as $m_1(\mathbf{z}_k|\mathbf{z}_0) = \mathcal{L}(f(\mathbf{z}_0, k), b)$, $e(\mathbf{z}_k|\mathbf{x}_k) = \mathcal{L}(h(\mathbf{x}_k), b)$, $p(\mathbf{z}_0) = \mathcal{L}(0, b)$, and $d(\mathbf{x}_k|\mathbf{z}_k) = \mathcal{L}(\zeta(\mathbf{z}_k), 1)$. Particularly, $m_1(\mathbf{z}_k|\mathbf{z}_0)$ has a fixed scale parameter b and a location parameter $f(\mathbf{z}_k)$ as a discretized dynamical system of Eq. 2:

$$\begin{aligned} \mathbf{z}_k &= f(\mathbf{z}_0, k) \\ &= [\phi_k, \mathbf{r}_k] \\ &= [\phi_0 + \omega k \Delta T, \exp(-\lambda k \Delta T) \odot \mathbf{r}_0], \end{aligned} \quad (7)$$

where ΔT is the step size.

The KL minimization problem in Eq. 4 can be transformed into an absolute error minimization problem (Eq. 8) since the Laplace distribution entropy is independent of the location

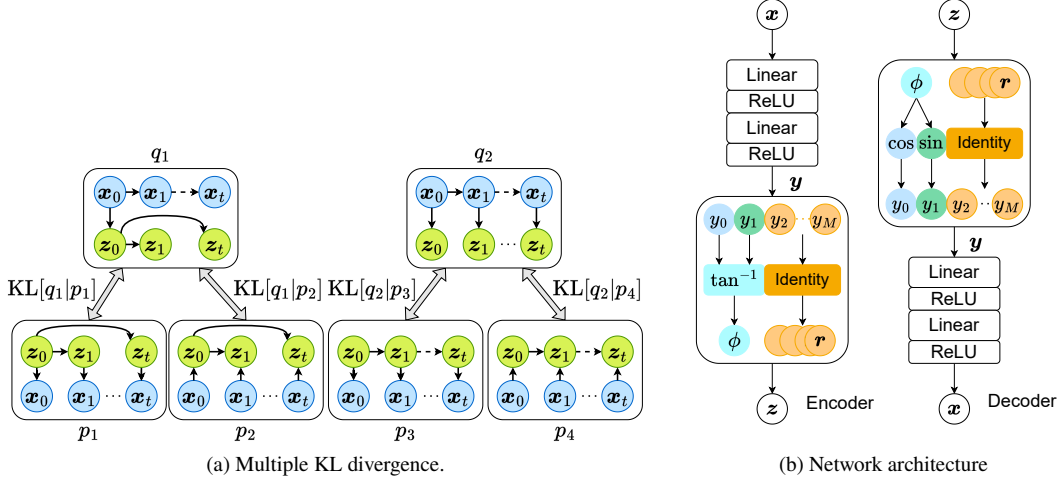


Figure 2. (a) Proposed probabilistic graphical models. Variational distributions q_1 and q_2 generate the latent variable z from observation x . Probabilistic distributions p_1 , p_2 , p_3 , and p_4 represent the target probabilistic model. We calculate four KL divergences to compare variational and probabilistic distributions. $KL[q_1|p_1]$ and $KL[q_1|p_2]$ represent transient process losses through the time expansion in latent space. $KL[q_2|p_3]$ and $KL[q_2|p_4]$ represent the stationary process losses directly derived from the observation space. (b) Network architecture of the encoder h and decoder z . Encoder input and decoder output are provided through the two-layer ReLU networks. The state variable x was encoded to the phase variable ϕ through using the inverse tangent \tan^{-1} . The other way around, the phase variable ϕ was decoded to the state variable x through using the sinusoidal functions \sin , and \cos .

parameters, and the distributions $q(\tau)$, $p(\tau)$ share a common distribution m_1 as:

$$\begin{aligned} KL[q|p] &= \mathbb{E}_q \left[\log \frac{e(z_0|x_0)}{p(z_0)} + \sum_{k=0}^T -\log d(x_k|z_k) \right] - H(\mathbf{X}) \\ &= \mathbb{E}_q \left[\frac{|z_0|}{b} + \sum_{k=0}^T |x_k - \zeta(z_k)| \right] \frac{-H(\mathbf{X}) - H(z_0|x_0) + \text{const}}{\text{constant for } h \text{ and } \zeta}, \end{aligned} \quad (8)$$

$$z_k = \begin{cases} h(x_0) + \epsilon_0 & \text{if } k = 0 \\ f(z_0, k) + \epsilon_k & \text{otherwise} \end{cases}, \epsilon_k \sim \mathcal{L}(\mathbf{0}, b), k \in \{0, \dots, T\}. \quad (9)$$

where $\mathbb{E}_{P(x)}[x] = \int_{\mathcal{X}} P(x)x dx$ is an expectation of the distribution $P(x)$ and $H(X) = \mathbb{E}_{P(X)}[-\log p(X)]$ is entropy. This objective function can be effectively minimized using the gradient descent method by employing reparameterization trick [26].

3.3. Learning Algorithm

In this section, we introduce the variational inference approach for efficient and stable learning of the encoder h and decoder z . The concrete algorithm is shown Alg. 1 that incorporates the following three ideas:

- (1) Define two types of distributions allowing the algorithm to satisfy both stationary and more transient objectives.
- (2) Introduce a λ -scaled discount factor to decay the error at a steady state. Because the observed data \mathbf{X} becomes close to a stationary distribution over time, the error decreases by the discount rate to improve the importance of the transient response.
- (3) Because the phase range is $\phi \in [0, 2\pi)$, the phase variable ϕ does not follow the Laplace

distribution \mathcal{L} and has a state jump from 2π to 0, causing unstable and inefficient learning procedures. Therefore, we define ϕ in a real number set \mathbb{R} . The variable ϕ was converted to 0 and 2π via the activation function of the encoder and decoder networks, as shown in Fig. 2 (b).

Algorithm 1 Learning Encoder/Decoder

Demonstration Data: \mathcal{D}
Hyper-Parameter: $\gamma, \omega, \lambda, |B|$
Learning network: h, ζ
while update times **do**
 Batch sample $\mathbf{B} \in \mathbb{R}^{|\mathbf{B}| \times T \times N}$ from \mathcal{D}
 Encoding $\mathbf{z}'_k \sim e(\mathbf{z}_k | \mathbf{x}_k), \mathbf{x}_k \sim \mathbf{B}$
 Rollout $\mathbf{z}_k \sim m_1(\mathbf{z}_k | \mathbf{z}_0)$
 Unwrap ϕ_k in \mathbf{z}_k and \mathbf{z}'_k
 Calculation Loss $L(h, \zeta; \mathbf{B})$
 Update Network for h, ζ
end while

3.3.1. Probabilistic Models

As shown in Fig. 2 (a), the following six probability distributions were defined:

$$q_1(\tau) = p(\mathbf{X}) \cdot e(\mathbf{z}_0 | \mathbf{x}_0) \cdot \prod_{k=1}^T m_1(\mathbf{z}_k | \mathbf{z}_0), \quad (10)$$

$$p_1(\tau) = p(\mathbf{z}_0) \cdot d(\mathbf{x}_0 | \mathbf{z}_0) \cdot \prod_{k=1}^T m_1(\mathbf{z}_k | \mathbf{z}_0) d(\mathbf{x}_k | \mathbf{z}_k), \quad (11)$$

$$p_2(\tau) = p(\mathbf{X}) \cdot e(\mathbf{z}_0 | \mathbf{x}_0) \cdot \prod_{k=1}^T m_2(\mathbf{z}_k | \mathbf{z}_0, \mathbf{x}_k), \quad (12)$$

$$q_2(\tau) = p(\mathbf{X}) \cdot \prod_{k=0}^T e(\mathbf{z}_k | \mathbf{x}_k), \quad (13)$$

$$p_3(\tau) = p(\mathbf{z}_0) \cdot d(\mathbf{x}_0 | \mathbf{z}_0) \cdot \prod_{k=1}^T m_1(\mathbf{z}_k | \mathbf{z}_{k-1}) d(\mathbf{x}_k | \mathbf{z}_k), \quad (14)$$

$$p_4(\tau) = p(\mathbf{X}) \cdot e(\mathbf{z}_0 | \mathbf{x}_0) \cdot \prod_{k=1}^T m_2(\mathbf{z}_k | \mathbf{z}_{k-1}, \mathbf{x}_k), \quad (15)$$

where q_\bullet denotes the variational distribution and p_\bullet denotes the model distribution, as defined in Section 3.2. Note that in data distribution $p(\mathbf{X})$, the stationary data \mathbf{x} on the closed-orbit occupancy than transient data far from the closed-orbit since the transition part almost converges to the origin during the data collection. Therefore, the batch sample for training is mainly sampled from stationary data. Here, the probability distribution q_1 plays a role in training the transient response. It sequentially generates k steps future latent variable \mathbf{z}_k from the initial state \mathbf{x}_0 . This process enhances the encoder e learning through the gradient backpropagation from future reconstruction loss, inducing sensitive learning against the transient response.

Conversely, Since distribution q_2 generates \mathbf{z}_k from each time observation \mathbf{x}_k , the backpropagation is limited around the local timestep. Consequently, learning how to reconstruct batch samples, i.e., the neighborhood of the closed orbit, is enhanced. The model m_1 is conditioned only by the initial latent variable \mathbf{z}_0 ; however, model m_2 is also conditioned by the observation \mathbf{x}_k at that time as:

$$m_2(\mathbf{z}_k | \mathbf{z}_0, \mathbf{x}_k) = \mathcal{L}(f(\mathbf{z}_0, k, \mathbf{x}_k), 1), \quad (16)$$

$$f(\mathbf{z}_0, k, \mathbf{x}_k) = f(\mathbf{z}_0, k) + \kappa(h(\mathbf{x}_k) - f(\mathbf{z}_0, k)), \quad (17)$$

where $\kappa \in [0, 1]$ is the intensity parameter. The model m_2 matches the transient responses of latent variable \mathbf{z}_k with the encoder function h of observation \mathbf{x}_k . The difference between the models p_1 and p_2 lies in the direction of the conditions (see directions of arrows in Fig. 2 (a)). Model p_1 represents the decoding probability from \mathbf{z} to \mathbf{x} , whereas model p_2 represents the filtering probability from \mathbf{x} to \mathbf{z} .

3.3.2. Scaled Absolute Error Minization

We derived the six absolute error loss functions from the four KL divergences $\text{KL}[q_1|p_1]$, $\text{KL}[q_1|p_2]$, $\text{KL}[q_2|p_3]$, and $\text{KL}[q_1|p_4]$ with two additional losses regarding the difference in the observable \mathbf{x} , as shown below:

$$L(h, \zeta; \mathbf{X}) = L_{\text{Rec}} + L_{\text{Enc}} + L_{\text{Dec}} + L_{\text{Lat}} + \sqrt{\Delta t} \cdot L_{\text{Rec,Diff}} + \sqrt{\Delta t} \cdot L_{\text{Dec,Diff}}, \quad (18)$$

$$L_{\text{Rec}} = \mathbb{E}_{q_1} \left[(1 - \gamma) \sum_{k=0}^T \gamma^k |\mathbf{x}_k - \zeta(\mathbf{z}_k)| \right], \quad (19)$$

$$L_{\text{Enc}} = \mathbb{E}_{q_1} \left[(1 - \gamma) \sum_{k=1}^T \gamma^k \kappa |\mathbf{c}_k \odot (h(\mathbf{x}_k) - f(\mathbf{z}_0, k))| \right], \quad (20)$$

$$L_{\text{Dec}} = \mathbb{E}_{q_2} \left[(1 - \gamma) \sum_{k=0}^T \gamma^k |\mathbf{x}_k - \zeta(\mathbf{z}'_k)| \right], \quad (21)$$

$$L_{\text{Lat}} = \mathbb{E}_{q_2} \left[(1 - \gamma) \sum_{k=1}^T \gamma^k (2 - \kappa) |\mathbf{c}_k \odot (h(\mathbf{x}_k) - f(\mathbf{z}'_{k-1}, 1))| \right], \quad (22)$$

$$L_{\text{Rec,Diff}} = \mathbb{E}_{q_1} \left[(1 - \gamma) \sum_{k=0}^{T-1} \gamma^k |\Delta(\mathbf{x}_{k+1}, \mathbf{x}_k) - \Delta(\zeta(\mathbf{z}_{k+1}), \zeta(\mathbf{z}_k))| \right], \quad (23)$$

$$L_{\text{Dec,Diff}} = \mathbb{E}_{q_2} \left[(1 - \gamma) \sum_{k=0}^{T-1} \gamma^k |\Delta(\mathbf{x}_{k+1}, \mathbf{x}_k) - \Delta(\zeta(\mathbf{z}'_{k+1}), \zeta(\mathbf{z}'_k))| \right], \quad (24)$$

\mathbf{z}_k is sampled from Eq.9,

$$\mathbf{z}'_k = h(\mathbf{x}_k) + \boldsymbol{\epsilon}_k, \boldsymbol{\epsilon}_k \sim \mathcal{L}(0, b),$$

$$\Delta(\mathbf{x}_{k+1}, \mathbf{x}_k) = \frac{\mathbf{x}_{k+1} - \mathbf{x}_k}{\Delta T},$$

$$\mathbf{c}_k = \frac{1 - \gamma \mathbf{d}}{1 - \gamma} \odot \mathbf{d}^k, \mathbf{d} = [1, \exp(-\lambda \Delta T)] \in \mathbb{R}^M,$$

where \odot represents element-wise multiplication, i.e., Hadamard product. Latent variables z_k and z'_k are generated by q_1 and q_2 , respectively, for Monte Carlo integration of the KL divergences. The latent variable z is a random variable that transitions through the phase amplitude Eq. 9, while z'_k is a time-invariant latent variable generated only by the encoder $h(\mathbf{x}_k)$. Additionally, because the velocity component is more critical in the dynamics model, $L_{\bullet, \text{Diff}}$ is added to calculate the error of the difference approximation between the reconstructed observed variable $\zeta(z)$ and observed variable \mathbf{x} in the data. Furthermore, the error is computed by exponential weighted averaging of γ and c_k . The discount factor γ commonly occurs in loss functions. The λ -scaled discount factor c_k decays the encoder error for each timestep k toward the future.

3.3.3. Structured Neural Network

Finally, we modified the activation function of the two-layered Perceptron, as shown in Fig. 5 (b). The phase variable ϕ is defined in \mathbb{R} , which converts the variables y_0 and y_1 into $(-\pi, \pi)$ in the last layer, and the decoder input layer converts ϕ into the circumference S^1 by activating functions \sin and \cos . Because the encoder output ϕ_k has a different range than \mathbb{R} , The phase-unwrapping process is applied to phase ϕ for the time evolution.

4. Experimental Setups

We conducted three experiments to confirm our contributions: 1) learning a dynamical system representation that can reproduce the transient response of the demonstration data, 2) end-effector tracking control using a simulated arm robot, and 3) imitation learning from human movement data on a real arm robot.

4.1. Simple Limit Cycle

First, we validated whether the proposed learning frameworks can reconstruct the transient response of a dynamical system with a simple limit cycle [27,28]:

$$\dot{\mathbf{x}} = \begin{bmatrix} 0 & -\omega \\ \omega & 0 \end{bmatrix} \mathbf{x} - (r^2 - \alpha)\mathbf{x}, \quad (25)$$

where the state $\mathbf{x} = [x, y] \in \mathbb{R}^2$, $r = |\mathbf{x}|$, $\alpha = 1$ is the scale parameter and $\omega = 2$ is the characteristic frequency of the limit cycle, as is depicted in Fig. 3 (a). Therefore, we can analytically derive the encoder function using the phase-amplitude equation with the observation function $\phi = \tan^{-1} \frac{y}{x}$, $z = \left(\frac{r^2 - \alpha}{r^2} \right)^{\frac{\lambda}{2\alpha}}$:

$$\begin{aligned} \dot{\phi} &= \omega, \\ \dot{z} &= -\lambda z, \end{aligned} \quad (26)$$

where $\omega > 0$ and $\lambda > 0$ are the characteristic frequency and exponent, respectively. The exponent λ can be defined with α as $\lambda = 2\alpha$.

4.2. Lemniscate tracking control

Second, we evaluate the motion generation and feedback mechanisms of the proposed method by comparing our method with the dynamic movement primitives (DMPs) method [29] in transient situations. Furthermore, we compared the reproducibility of the 6DOF single-arm robot end-effector movement in a lemniscate tracking task.

The demonstration data were collected through the 6DoF arm robot tracking task using a physics simulation, as shown in Fig. 4 (a). First, we solved the inverse kinematics problem and derived the target joint angles that correspond to the lemniscate end-effector trajectory. Then, we used a proportional and derivative (PD) servo control to track the target joint angles. The dynamics representation of the movement trajectories was learned from the demonstration data, and the observable \mathbf{x} was reconstructed as shown in Table 2. The characteristic frequencies were estimated using autocorrelation analysis and the characteristic exponents were obtained for 32 points on a logarithmic scale from the range listed in Table 1. Subsequently, the PD servo follows the trajectory generated by the learned latent system with interactive feedback, as shown in Eq. 3.

4.3. Human movement imitation

Finally, we conducted a human movement imitation task using a real 6DoF arm robot as shown in Fig. 5 (b). A motion capture system measures the baton swing movement and our proposed method reconstructed the human movement trajectory of the baton. Subsequently, the decoded state of the acquired latent dynamics was used to generate the robot arm movement trajectory. The real arm robot tracked the generated position and orientation from the learned latent system in the hand coordinate system with the feedback connection with the marker position on the baton attached on the robot as shown in Eq. 3.

Table 2 lists the observables to learn latent dynamics. The motion-captured trajectories were the positions of the baton, which a human conducts with a 3-beat rhythm for 24 s. Its tempos are 30 times per 60 s. As a preprocessing step, the trajectories were low-pass filtered with a cutoff frequency of 5 Hz and standardized by removing the mean and variance. The characteristic frequencies were estimated from the autocorrelation analysis results of the acquired data. The characteristic exponents were obtained from 512 samples in the range listed in Table 1 on a logarithmic scale. The sampling rate of the motion capture system was 360 Hz, and the control period for the real robot arm UR5e was 10 Hz. Furthermore, our control system is a CPU-only PC (Intel Core i7-3770K CPU @ 3.5 GHz, Memory 20 GB) without GPU because the integral process to predict the future state becomes redundant owing to the use of the analytical solution of the latent dynamical system.

5. Results

5.1. Simple Limit Cycle

We generated 500 trajectories from the randomly sampled initial positions using Eq. 25 and learned the encoder and decoder with 250 trajectories as a train-set. Table 1 lists other learning parameters. The learned vector field shown in Fig. 3 (b) reconstructs the steady orbit and transient response around the limit cycle. We evaluated the root mean square error (RMSE), $\sqrt{1/T \sum_{k=0}^T \|\mathbf{x}_k - \zeta(\mathbf{z}_k)\|_2^2}$, with the test set; these were not used in the network training process. The proposed method successfully reconstructed the original dynamics in Eq. 25.

Table 1. Parameter List

Parameters	Experiment name	Values	Notes
Optimizer		Adam	
Learning rate		10^{-3}	
Batch size B		255	
Num. iteration N	Simple limit cycle	5000	
	Lemniscate follow	5000	
	Human-to-Robot	10000	
Data lengths	Simple limit cycle	5000	
	Lemniscate follow	400	
	Human-to-Robot	8700	3 beats, 24 s
Split horizon T	Simple limit cycle	500	
	Lemniscate follow	300	
	Human-to-Robot	2120	
Discount factor γ	Simple Limit Cycle	0.99	
	Lemniscate follow	0.999	
	Human-to-Robot	0.99976	$= \exp(-\frac{\Delta T \omega}{2\pi}/2)$
MLP hidden layer size		[512, 512]	
Laplace's scale b		10^{-5}	
Intensity parameter κ		0.5	
Feedback gain g	Simple limit cycle	-	
	Lemniscate follow	$5 \times 10^{-2} / 1 \times 10^{-3}$	Anomaly / Other
	Human-to-Robot	10^{-4}	
Discrete step ΔT	Simple limit cycle	0.02 s	
	Lemniscate follow	0.050 s	
	Human-to-Robot	0.050 / 0.003 s	UR5e / Mocap
Dim. latent $ z $	Simple limit cycle	2	
	Lemniscate follow	32	
	Human-to-Robot	512	
Characteristic freq. ω	Simple limit cycle	2.00 rad/s	
	Lemniscate follow	0.2 Hz	
	Human-to-Robot	0.17 Hz	3 beats
Characteristic exponents Range $[\lambda_{\min}, \lambda_{\max}]$	Simple limit cycle	[2.0, 2.0] 1/s	$= 2\alpha$
	Lemniscate follow	[0.039, 6.283] 1/s	
	Human-to-Robot	[0.06, 11.31] 1/s	

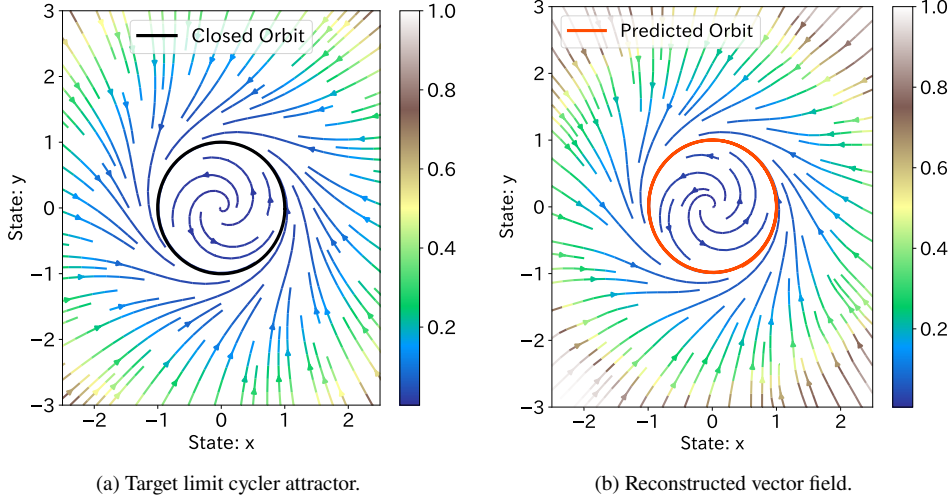


Figure 3. Simple limit cycle system. (a) Target limit cycle attractor. Color bar shows the normalized norm of the vector fields: $\dot{\mathbf{x}} = F(\mathbf{x})$ and a solid line shows the limit cycle. (b) Reconstructed vector field. Color bar shows the normalized norm of the vector fields: $\dot{\mathbf{x}} = \frac{\partial \mathcal{L}}{\partial \mathbf{z}} f(\mathbf{z})$, $\mathbf{z} = h(\mathbf{x})$. Red line denotes the closed orbit after 1.8 s (= 100 timesteps.)

5.2. Lemniscate tracking control

We considered four transient movement situations to validate our proposed method. First, we conducted the control task in an anomaly situation in which the control signal was suddenly stopped for six seconds. The feedback mechanism in Eq. 3 was effectively worked to synchronize the latent variable with the actual robot state, as shown in Fig. 4 (b). Without the feedback term, the robot rapidly attempted to return to the target state after the control was recovered, causing the behavior that deviated significantly from the demonstration. Conversely, the proposed method stopped the latent phase based on the feedback of the robot’s encoder when the control signal was lost. After restoring the control, the robot gently followed the demonstrated trajectory.

Second, we compared the robustness against the force noise (100N) at the end-effector with DMP. Because the proposed method models the amplitude components dynamics, it can be generated to converge quickly behavior to the demonstrated trajectory, compared to the DMP generated dynamics, as shown in Fig. 4 (d) and Fig. 4 (g). The RMSE score between the proposed method and the demonstration was superior to that of the DMPs, as shown in Fig. 4(c).

Third, we considered the slow-motion task that forces the robot to decrease the tracking speed in half. Because the time transition part and observation space are entirely separated, the proposed method makes it straightforward to scale the phase of the limit cycle. The trajectory-following shape dynamics are shown in Figs. 4 (e) and 4 (h). Because the phase and amplitude components are not separated in DMP, the waveform collapses along the slow phase.

Fourth, we considered the reshaping task that imposes the robot shrinkage of the size of the limit cycle in half. Here, the proposed method shrinks the waveform’s shape while preserving the phase, whereas the DMP is slightly delayed in phase, as shown in Fig. 4 (f) and Fig. 4 (i). The RMSE scores of the third and force task between the proposed method and the demonstration were superior to that of the DMPs, as shown in Fig. 4 (c). Although slow-motion and reshaping tasks were achieved based on orientation-preserving homeomorphism proposed by [10], it is difficult to reproduce the same in the dynamic domain because the multi-DoF dynamics has a complex interaction. Nonetheless, our approach based on the phase-amplitude equation can be applied to the scaling task with orientation-preserving homeomorphism.

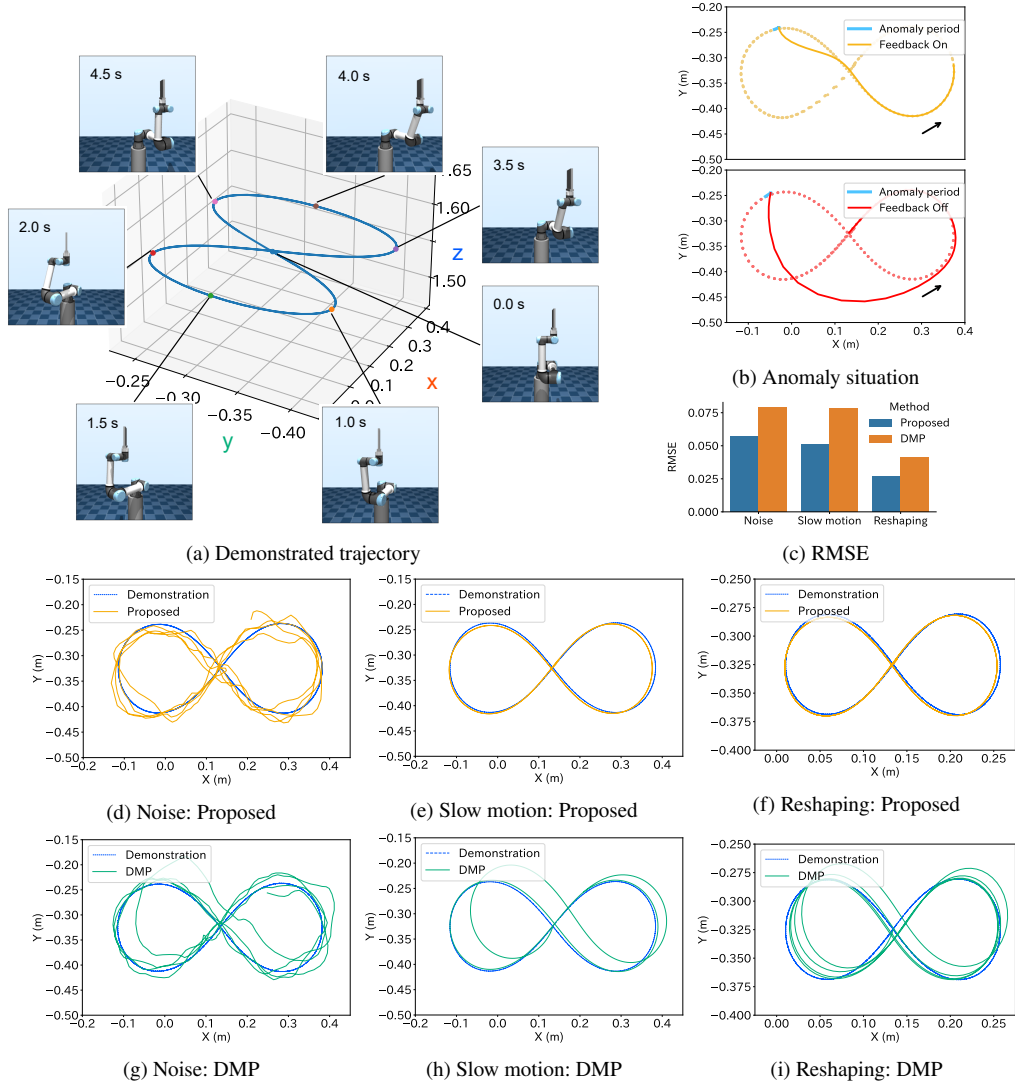


Figure 4. Lemniscate tracking tasks: anomaly situation Fig. (b), force noise injection Fig. (c, d, g), slow motion (c, e, h), and trajectory reshaping Fig. (c, f, i). The demonstration data was generated in the lemniscate curve with a constant frequency of 0.2 Hz for 20 s.

Table 2. Observable x List

Simple Limit Cycle
$[x, y] \in \mathbb{R}^2$
Lemniscate Following
Tool Center Position in \mathbb{R}^3
Tool Center Velocity in \mathbb{R}^3
Human-to-Robot
The head and tail position of the rod in \mathbb{R}^6
The head and tail velocity of the rod in \mathbb{R}^6

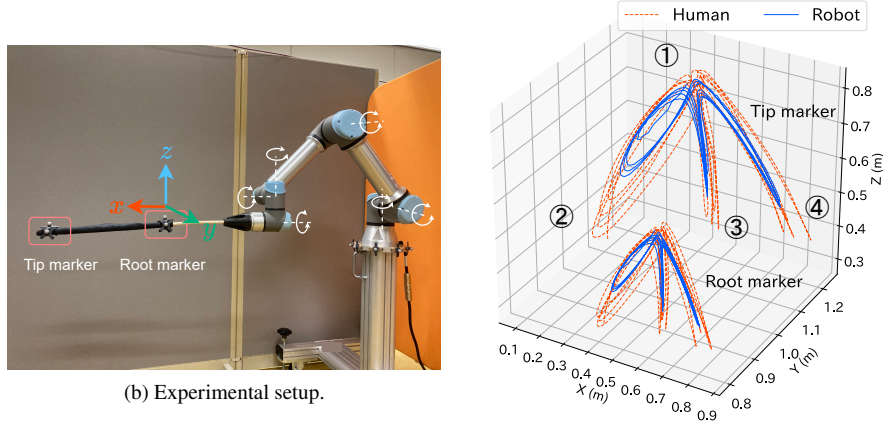
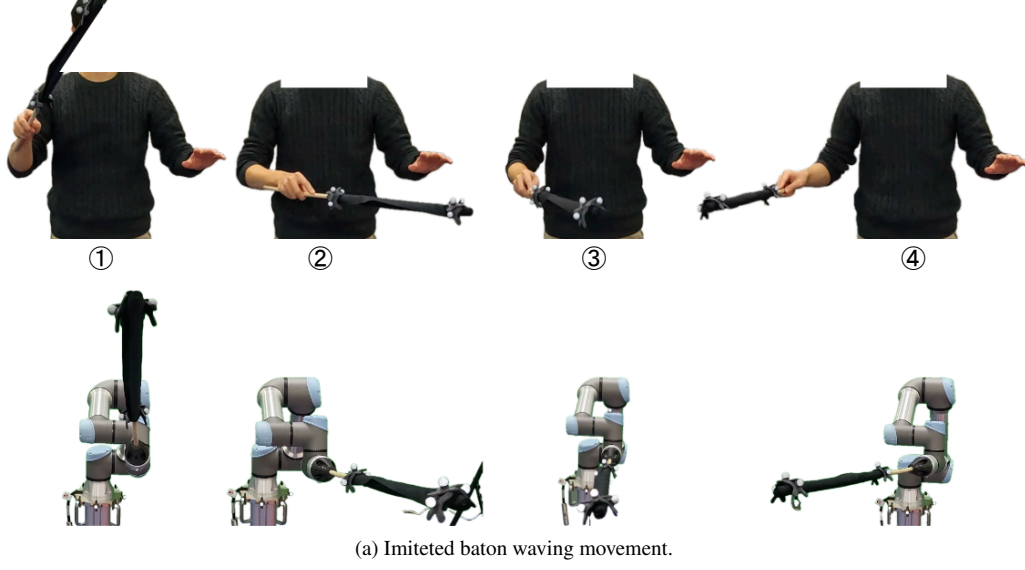


Figure 5. Imitation learning experiment. a) Baton waving with three beats and 30 tempos per 60 s. b) Robot arm system with markers to capture movements. c) Generated baton motions by a human and a robot arm. Marker positions attached to the tip and root of the baton are plotted. The arm robot successfully imitated the demonstrated human baton-waving motion.

5.3. Human movement imitation

Figure 5 (a) depicted the snapshot of the imitated movement when the robot follows the decoded trajectory generated by the latent dynamics learned from the human baton waving motion. The learned model properly reconstructed the human trajectory, despite the original human behavior being perturbed around a limited cycle. The reconstructed trajectory was tracked by the arm robot using a servo controller. The resulting movement of the robot was measured by a motion capture system using markers put on the robot (Fig. 5 (b)) As plotted in Fig. 5 (c), the robot arm successfully imitated the human baton waving motion. This result indicates that the learned model was able to extract the stable orbit and the transient response.

6. Conclusion

We introduced a novel framework for learning forward and inverse mappings to a phase-amplitude dynamics, enabling imitation learning in movement tasks from human to robot. Additionally, we developed an interactive feedback control mechanism to cope with external disturbance or anomaly situations. Our proposed method was validated through two simulation experiments and a real imitation learning experiment. Consequently, the acquired latent dynamic model by our proposed method successfully reproduced the steady-state response near the limit cycle and the transient response; moreover, a 6DoF arm robot replicated the human rhythmic motion.

With the proposed method, our learning system cannot imitate attractors with a torus structure or human behavior of switching between multiple attractors. For example, in a complex assembly task, a human would switch attractors sequentially while having the left and right arms generate separate attractors. To cope with this kind of situation, as a future study, we consider training multiple networks to integrate different attractor dynamics.

Appendix

Loss Function Derivation

Here we derive the absolute error loss from the KL divergence in Eqs. 10-15. The loss functions $\text{KL}[q_1|p_1]$, $\text{KL}[q_1|p_2]$, $\text{KL}[q_2|p_3]$, $\text{KL}[q_1|p_4]$ were derived using an approach similar to that in Subsection 3.2 as follows: The first KL divergence $\text{KL}[q_1|p_1]$ is equivalent to the Eq. 8, except for the β parameter of VAE. Therefore, the derivation is also the same.

$$\begin{aligned}\text{KL}[q_1|p_1] &= \mathbb{E}_{q_1} \left[-\beta \log p(z_0) + \sum_{k=0}^T -\log d(\mathbf{x}_k|z_k) \right] + \text{const} \\ &= \mathbb{E}_{q_1} \left[\frac{\beta}{b} |z_0| + \sum_{k=0}^T |\mathbf{x}_k - \zeta(z_k)| \right] + \text{const.}\end{aligned}\quad (27)$$

The second KL loss $\text{KL}[q_1|p_2]$ is derived as follows:

$$\begin{aligned}\text{KL}[q_1|p_2] &= \mathbb{E}_{q_1} \left[\sum_{k=1}^T \log m_1(z_k|z_0) - \sum_{k=1}^T \log m_2(z_k|z_0, \mathbf{x}_k) \right] + \text{const} \\ &= \mathbb{E}_{q_1} \left[\sum_{k=1}^T |z_k - f(z_0, \mathbf{x}_k, k)| \right] + \text{const} \\ &\leq \mathbb{E}_{q_1} \left[\sum_{k=1}^T \kappa |h(\mathbf{x}_k) - f(z_0, k)| + |\epsilon_k| \right] + \text{const.}\end{aligned}\quad (28)$$

Note that the Laplace distribution entropy $\mathbb{E}_{m_1}[-\log m_1] = 1 + \log(2b)$ is independent of the location parameter $f(z_0, k)$. Moreover, the last inequality is based on the following formula-

tion:

$$\begin{aligned}
z_k - f(z_0, \mathbf{x}_k, k) &= f(z_0, k) + \epsilon_k - f(z_0, k) - \kappa(h(\mathbf{x}_k) - f(z_0, k)) \\
&= -\kappa(h(\mathbf{x}_k) - f(z_0, k)) + \epsilon_k \\
|z_k - f(z_0, \mathbf{x}_k, k)| &\leq \kappa|h(\mathbf{x}_k) - f(z_0, k)| + |\epsilon_k|.
\end{aligned} \tag{29}$$

The third KL loss can be expanded as follows:

$$\begin{aligned}
\text{KL}[q_2|p_3] &= \mathbb{E}_{q_2} \left[-\beta \log p(z_0) - \sum_{k=1}^T \log m_1(z_k|z_{k-1}) - \sum_{k=0}^T \log d(\mathbf{x}_k|z_k) \right] \\
&\quad + \text{const} \\
&= \mathbb{E}_{q_2} \left[\beta \frac{|z_0|}{b} + \sum_{k=1}^T |z_k - f(z_{k-1}, 1)| + \sum_{k=0}^T |\mathbf{x}_k - \zeta(z_k)| \right] \\
&\quad + \text{const} \\
&\leq \mathbb{E}_{q_2} \left[\sum_{k=1}^T |h(\mathbf{x}_k) - f(z_{k-1}, 1)| + \sum_{k=0}^T |\mathbf{x}_k - \zeta(z_k)| \right] \\
&\quad + \mathbb{E}_{q_2} \left[\beta \frac{|z_0|}{b} + \sum_{k=1}^T |\epsilon_k| \right] + \text{const.}
\end{aligned} \tag{30}$$

Here, the entropy term $\mathbb{E}_e[-\log e] = 1 + \log(2b)$ is also independent of the encoder h . The last inequality is based on the following formulation:

$$\begin{aligned}
z_k - f(z_{k-1}, 1) &= h(\mathbf{x}_k) + \epsilon_k - f(z_{k-1}, 1) \\
|z_k - f(z_{k-1}, 1)| &\leq |h(\mathbf{x}_k) - f(z_{k-1}, 1)| + |\epsilon_k|.
\end{aligned} \tag{31}$$

The fourth KL Loss function is derived as follows.

$$\begin{aligned}
\text{KL}[q_2|p_4] &= \mathbb{E}_{q_2} \left[-\sum_{k=1}^T \log m_2(z_k|z_{k-1}, \mathbf{x}_k) \right] + \text{const} \\
&= \mathbb{E}_{q_2} \left[\sum_{k=1}^T |z_k - f(z_{k-1}, \mathbf{x}_k, 1)| \right] + \text{const} \\
&\leq \mathbb{E}_{q_2} \left[\sum_{k=1}^T (1 - g)|h(\mathbf{x}_k) - f(z_{k-1}, 1)| + |\epsilon_k| \right] + \text{const.}
\end{aligned} \tag{32}$$

We repeatedly use the encoder's entropy independence of the location parameter. The final inequality is based on the following formulation:

$$\begin{aligned}
z_k - f(z_{k-1}, \mathbf{x}_k, 1) &= z_k - f(z_{k-1}, 1) - \kappa(h(\mathbf{x}_k) - f(z_{k-1}, 1)) \\
&= h(\mathbf{x}_k) + \epsilon_k - f(z_{k-1}, 1) - \kappa(h(\mathbf{x}_k) - f(z_{k-1}, 1)) \\
&= (1 - \kappa)(h(\mathbf{x}_k) - f(z_{k-1}, 1)) + \epsilon_k \\
&\leq (1 - \kappa)|h(\mathbf{x}_k) - f(z_{k-1}, 1)| + |\epsilon_k|.
\end{aligned} \tag{33}$$

7. Acknowledgments

This study used several open-source software projects, such as PyTorch [30], MuJoCo Menagerie [31], dm-control [32], and DMP code collection [33]. We are grateful to the project contributors for providing valuable machine-learning tools.

8. Funding

This work was supported by JSPS; under KAKENHI [Grant number 19J22987], NEDO under [project JPNP20006]; JST under Moonshot R&D program [Grant number JPMJMS223B-3], and Tateisi Science and Technology Foundation.

9. Disclosure statement

No potential conflict of interest was reported by the author(s).

References

- [1] Schaal S. Learning from demonstration. In: Mozer M, Jordan MI, Petsche T, editors. *Advances in Neural Information Processing Systems*; Vol. 9; Denver, Colorado, USA; 1996. p. 1040–1046.
- [2] Ravichandar H, Polydoros AS, Chernova S, et al. Recent advances in robot learning from demonstration. *Robotics, and Autonomous Systems*. 2020;3(1):297–330.
- [3] Hussein A, Gaber MM, Elyan E, et al. Imitation learning: A survey of learning methods. *ACM Computing Surveys*. 2017;50(2).
- [4] Miyamoto H, Schaal S, Gandolfo F, et al. A kendama learning robot based on bi-directional theory. *Neural Networks*. 1996;9(8):1281–1302.
- [5] Mülling K, Kober J, Kroemer O, et al. Learning to select and generalize striking movements in robot table tennis. *The International Journal of Robotics Research*. 2013;32(3):263–279.
- [6] Pahič R, Ridge B, Gams A, et al. Training of deep neural networks for the generation of dynamic movement primitives. *Neural Networks*. 2020;127:121–131.
- [7] Chi C, Feng S, Du Y, et al. Diffusion policy: Visuomotor policy learning via action diffusion. In: *Proceedings of Robotics: Science and Systems*; Daegu, Republic of Korea; 2023.
- [8] Florence P, Lynch C, Zeng A, et al. Implicit behavioral cloning. In: Faust A, Hsu D, Neumann G, editors. *Proceedings of the Conference on Robot Learning*; Vol. 164; London, UK; 2021. p. 158–168.
- [9] Yang PC, Sasaki K, Suzuki K, et al. Repeatable folding task by humanoid robot worker using deep learning. *IEEE Robotics and Automation Letters*. 2017;2(2):397–403.
- [10] Ijspeert AJ, Nakanishi J, Hoffmann H, et al. Dynamical movement primitives: Learning attractor models for motor behaviors. *Neural Computation*. 2013;25(2):328–373.
- [11] Saveriano M, Abu-Dakka FJ, Kramberger A, et al. Dynamic movement primitives in robotics: A tutorial survey. *The International Journal of Robotics Research*. 2023;42(13):1133–1184.
- [12] Kuramoto Y. *Chemical oscillations, waves, and turbulence*. Springer Berlin, Heidelberg; 2003. Springer Series in Synergetics.
- [13] Shirasaka S, Kurebayashi W, Nakao H. Phase-amplitude reduction of limit cycling systems. In: Mauroy A, Mezić I, Susuki Y, editors. *The koopman operator in systems and control: Lecture notes in control and information sciences*. Vol. 484. Springer Cham; 2020. p. 383–417.
- [14] Schaal S. Is imitation learning the route to humanoid robots? *Trends in cognitive sciences*. 1999; 3(6):233–242.
- [15] Morimoto J, Endo G, Nakanishi J, et al. A biologically inspired biped locomotion strategy

- for humanoid robots: Modulation of sinusoidal patterns by a coupled oscillator model. *IEEE Transactions on Robotics*. 2008;24(1):185–191.
- [16] Kramberger A, Shahriari E, Gams A, et al. Passivity based iterative learning of admittance-coupled dynamic movement primitives for interaction with changing environments. In: *IEEE/RSJ International Conference on Intelligent Robots and Systems*; Madrid, Spain; 2018. p. 6023–6028.
 - [17] Katayama T. Subspace methods for system identification. 1st ed. Springer London; 2005.
 - [18] Brunton SL, Kutz JN. Data-driven science and engineering: Machine Learning, dynamical systems, and control. 2nd ed. Cambridge University Press; 2022.
 - [19] Lawrence ND. Gaussian process latent variable models for visualisation of high dimensional data. In: Thrun S, Saul LK, Schölkopf B, editors. *Advances in Neural Information Processing Systems*; Vol. 16; Vancouver and Whistler, British Columbia, Canada; 2003. p. 329–336.
 - [20] Wang JM, Fleet DJ, Hertzmann A. Gaussian process dynamical models. In: *Advances in Neural Information Processing Systems*; Vol. 18; Vancouver, British Columbia, Canada; 2005. p. 1441–1448.
 - [21] Ghahramani Z, Roweis ST. Learning nonlinear dynamical systems using an EM algorithm. In: Kearns MJ, Solla SA, Cohn DA, editors. *Advances in Neural Information Processing Systems*; Vol. 11; Denver, Colorado, USA; 1998. p. 431–437.
 - [22] Khansari-Zadeh SM, Billard A. Learning stable nonlinear dynamical systems with gaussian mixture models. *IEEE Transactions on Robotics*. 2011;27(5):943–957.
 - [23] Umlauf J, Hirche S. Learning stable stochastic nonlinear dynamical systems. In: Precup D, Teh YW, editors. *Proceedings of the International Conference on Machine Learning*; Vol. 70; Sydney, Australia; 2017. p. 3502–3510.
 - [24] Calinon S, Li Z, Alizadeh T, et al. Statistical dynamical systems for skills acquisition in humanoids. In: *IEEE-RAS International Conference on Humanoid Robots*; Osaka, Japan; 2012. p. 323–329.
 - [25] Han Y, Xie M, Zhao Y, et al. On the utility of koopman operator theory in learning dexterous manipulation skills. In: *Proceedings of the Conference on Robot Learning*; Vol. 229; Atlanta, USA; 2023. p. 106–126.
 - [26] Higgins I, Matthey L, Pal A, et al. Beta-VAE: Learning basic visual concepts with a constrained variational framework. In: *International Conference on Learning Representations*; Toulon, France; 2017.
 - [27] Martin B. Differential equations and their applications: An introduction to applied mathematics. 2nd ed. Springer New York; 1993.
 - [28] Strogatz SH. Nonlinear dynamics and chaos: With applications to physics, biology, chemistry, and engineering. 2nd ed. CRC Press; 2015.
 - [29] Peternel L, Noda T, Petrič T, et al. Adaptive control of exoskeleton robots for periodic assistive behaviours based on EMG feedback minimisation. *PLOS ONE*. 2016;11(2):1–26.
 - [30] Paszke A, Gross S, Massa F, et al. PyTorch: An imperative style, high-performance deep learning library. In: Wallach H, Larochelle H, Beygelzimer A, et al., editors. *Advances in Neural Information Processing Systems*; Vol. 32; Vancouver, British Columbia, Canada; 2019. p. 8024–8035.
 - [31] Zakka K, Tassa Y, MuJoCo Menagerie Contributors. MuJoCo Menagerie: A collection of high-quality simulation models for MuJoCo ; 2022. Available from: https://github.com/google-deepmind/mujoco_menagerie.
 - [32] Tunyasuvunakool S, Muldal A, Doron Y, et al. dm_control: Software and tasks for continuous control. *Software Impacts*. 2020;6:100022.
 - [33] Peternel L. DMP codes collection: dmp-periodic [Computer software] ; 2021. Available from: <https://gitlab.com/dmp-codes-collection/dmp-periodic>.